Deformation-tolerant metal anodes for flexible sodium–air fiber batteries

Lei Ye,[1+] Xiangran Cheng,[1+] Meng Liao,[1] Tiancheng Zhao,[1] Xinlin Huang,[1] Xinyue Kang,[1] Kun Zhang,[1] Xuemei Sun,[1] Bingjie Wang,[1]* Huisheng Peng[1]*

Materials. Sodium metal (Na, 99.8%), sodium trifluoromethanesulfonate (NaTF, CF_3SO_3Na, 98%), diethylene glycol dimethyl ether (diglyme, $C_6H_{14}O_3$, 99.5%), trimethylolpropane ethoxylate triacrylate (average Mn of ~428), poly(vinylidene fluoride-co-hexafluoropropylene (average Mn of ~130000), and 2-hydroxy-2-methylpropiophenone ($C_{10}H_{12}O_2$, 97%) were purchased from Sigma-Aldrich Co. Ltd. Ethanol (C_2H_6O, 99.7%) and sodium iodide (99%) were obtained from Sinopharm Co. Ltd. Ferrocene ($C_{10}H_{10}Fe$, 99%), thiophene (C_4H_4S, 99%) and N-methyl-2-pyrrolidinone (C_5H_9NO, 99.9%) were purchased from Aladdin Co. Ltd. Parafilm was purchased from Bemis Co. Ltd. Celgard 2400 separator was purchased from Celgard Co. Ltd. Heat shrinkable tube was purchased from Suzhou Dasheng Materials Tech Co. Ltd.

Preparation of carbon nanotube film. Carbon nanotube (CNT) film used in this work was prepared by a floating catalyst chemical vapor deposition method. A composite catalyst of ferrocene (2 *wt%*) and thiophene (2 *wt%*) was well-dispersed in the ethanol carbon source and pumped into the furnace at a steady flow rate of 10 $mL \cdot h^{-1}$. Meanwhile, the mixture of hydrogen and argon (4:1, *v/v*) was flowed across the furnace at a rate of 1500 sccm. Then the ethanol was decomposed to produce carbon atom and generated CNT in the reducing atmosphere of hydrogen under the above synthetic condition. Finally, the CNT was blown to the bottom of furnace by the gas and pulled out with a stick. After a water coagulation bath for contraction, the CNT was wound around the roller and dried in the ambient air to form a porous CNT film. The resulting CNT film was composed of CNT bundles with a relatively high length of ~100 μm and exhibited macroscopically aligned structure.

Fabrication and electrochemical measurements of sodiated CNT layer protected Na fiber electrodes. To prepare sodiated CNT layer (SCL)/Na composite fiber electrodes, the Na metal fiber was wrapped with flexible CNT film and wetted with the electrolyte of 1 M NaTF in diglyme in an argon-filled glove box (H_2O < 0.1 ppm, O_2 < 0.1 ppm). The SCL was obtained *via* the physical contact and spontaneous reaction between metallic Na and CNT, driven by the difference in their Fermi levels. To evaluate the anodic electrochemical performance, symmetric cells from SCL/Na and bare Na fiber electrodes were assembled. Each cell was assembled with ~30 μL electrolyte of 1 M NaTF in diglyme and Celgard 2400 as separator in an argon-filled glove box (H_2O < 0.1 ppm, O_2 < 0.1 ppm). The electrolyte was dried with molecular sieves (4A) for 24 h before use. To investigate the cycling stability, the symmetric cells were tested under a galvanostatic plating and stripping process on a LAND-CT2001A battery tester. The unique one-dimensional Na fiber anode with a small diameter enabled the resultant battery a high utilization ratio of Na metal. The electrochemical impedance spectroscopy was measured on a CHI 660D electrochemical workstation with a frequency range from 0.01 Hz to 100 kHz and an amplitude of 5 mV. The open-circuit potential was set as the initial voltage. The rate performance was tested under increasing current densities from 1 to 8 $mA \cdot cm^{-2}$ at a given capacity of 1 $mAh \cdot cm^{-2}$.

Fabrication and electrochemical performance tests of Na–air fiber battery. The SCL/Na–air fiber battery exhibited a co-axial structure with a SCL/Na fiber as the anode, a flexible CNT film as the cathode, and a layer of gel electrolyte as the electrolyte as well as separator. The fabrication process comprised the following steps: Firstly, sodium metal fiber was wrapped with a CNT film. Then, the composite anode was dipped into a precursor solution composed of three components (solution A, B and

C), and exposed to ultraviolet irradiation for 15 s to form the gel electrolyte. The coating process was repeated at least three times until the anode was totally covered. The gel electrolyte-coated anode was immersed in Solution D for 12 h. Here, NaTF (1.75 g) was dissolved in diglyme (10 mL) to form Solution A. Poly(vinylidene fluoride-co-hexafluoropropylene (1 g) was dissolved in N-methyl-2-pyrrolidinone (4 g) to form Solution B. 2-Hydroxy-2-methylpropiophenone (0.01 g) was added to trimethylolpropane ethoxylate triacrylate (3 g) to form solution C. Sodium iodide (0.075 g) and NaTF (1.75 g) were dissolved in diglyme (10 mL) to form Solution D. Solution A, B and C were mixed by mass ratios of 4:5:3 to prepare the precursor solution of gel electrolyte. All the above samples were prepared in an argon-filled glove box (H_2O < 0.1 ppm, O_2 < 0.1 ppm). Then the gel electrolyte-coated SCL/Na fiber anode was taken out from the glove box and wrapped with a CNT film air cathode with a mass load of 28.2 μg. Finally, the fiber battery was encapsulated by low-density polyethylene, Parafilm and heat-shrinkable tube in sequence, which allowed the stable battery operation in air due to the prevented corrosion by moisture/carbon dioxide in air. For comparison, the bare Na–air fiber batteries without SCL was also fabricated. The Na-air fiber batteries were tested with a fixed capacity mode, in which the specific capacity was 500 $mAh \cdot g^{-1}$ and the current density was 1000 $mA \cdot g^{-1}$. The specific capacity (C) was calculated by $C=(I \times t)/m$, where I, t and m represented the discharge/charge current, discharge/charge time and the mass of the air cathode, respectively.

Fabrication and tests of self-powering strain-sensing system. The self-powering strain-sensing system was constructed with an energy harvesting unit of fiber solar cell, an energy storage unit of fiber Na–air battery and a fiber strain sensor. The fiber solar

cell was assembled by twisting the Ti/TiO_2 photo-anode and CNT counter electrode and sealing them in a heat-shrinkable tube filled with the I^-/I_3^- electrolyte. The fiber strain sensor was assembled by winding an elastic rubber fiber with polypropylene fibers to form a spring-like polypropylene fiber and coating the spring fiber substrate with CNT conductive ink. The current density-voltage curve of fiber solar cell was tested by Newport solar simulator (Oriel Sol 3A, 450 W Xe lamp) under AM 1.5 irradiation (100 $mW \cdot cm^{-2}$) and recorded by a Keithley 2400 source meter. The sensing response of fiber sensor was tested on a CHI 660D electrochemical workstation.

Finite Element Method Simulations. The Na plating process ($Na^+ + e^- \rightarrow Na$) was simulated by COMSOL Multiphysics 5.4 based on the finite element method. Two physics modules used were "Electrodeposition, Tertiary Nernst-Planck" and "Deformed Geometry interfaces". The models for cross-sections of Na-air fiber batteries were established and simulated. For the SCL/Na–air fiber battery, the radius of Na fiber anode and the thickness of gel electrolyte were both set as 1 mm. The wavy line indicated the flexible interface between SCL and Na fiber anode. For the bare Na–air fiber battery, the sharp protrusions indicated the cracks and creases formed on bare Na fiber anode during deformation. For the planar Na–air battery, the thickness of gel electrolyte was set as 1 mm. The initial Na^+ concentration in the electrolyte was set as 1 M. The exchange current density was set to be 1 $A \cdot m^{-2}$. Diffusion coefficient of Na^+ in the electrolyte was set as 10^{-9} $m^2 \cdot s^{-1}$. The ionic mobility, μ, was calculated with Nernst–Einstein relation. The voltage excitation between the anode and cathode was set as 2 V, and the remaining boundaries were set to be insulated. The concentration-dependent Bulter–Volmer equation was used to describe the reaction of Na deposition on the electrode surface.

Characterizations. SCL/Na and bare Na fiber electrodes were extracted from the CR2032 coin cells, washed with diglyme solvent three times to remove residual electrolyte and dried for 12 h in an argon-filled glove box (H_2O < 0.1 ppm, O_2 < 0.1 ppm) before characterizations. The structures were characterized by scanning electron microscope (SEM, Zeiss Gemini SEM500 FESEM operated at 5 kV), transmission electron microscopy (TEM, JEOL JEM-2100F operated at 200 kV), X-ray diffraction (XRD, Bruker AXS D8), Raman spectroscopy (Dilor LabRam-1B, He-Ne laser of 4 mW, excitation wavelength of 532 nm), Fourier transform infrared spectrum (FTIR, NICOLET 6700), X-ray photoelectron spectroscopy (XPS, PHI 5000C&PHI5300, Mg, 250 W, 14 kV), and automatic specific surface area and porosity analyzer (Quadrasorb evo). The electrochemical performances were tested on the LAND-CT2001A battery tester and CHI 660D electrochemical workstation. The optical photographs were taken by a camera (Nikon J1). The air-sensitive samples were sealed in an argon-filled boxer and quickly transferred into the chambers of test instrument before characterization. For XRD tests, the samples were sealed in the Kapton film to avoid side reactions with the air.

Results and Discussions

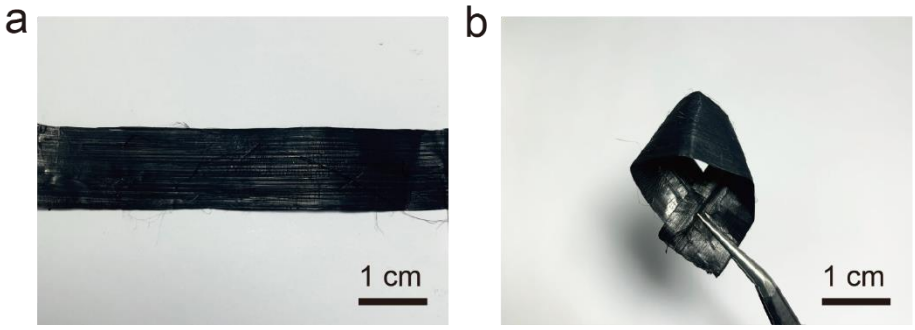

Fig. S1. (a) and (b) Photographs of CNT film.

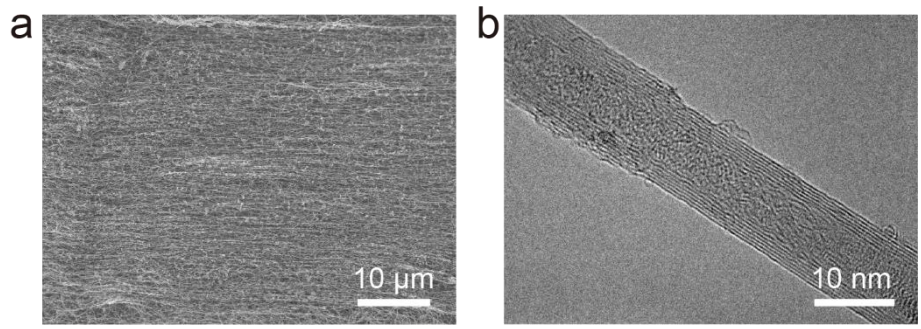

Fig. S2. (a) and (b) SEM and TEM images of the CNT film, respectively. The highly aligned CNT bundles were about 100 μm long. The CNT film exhibited a multi-walled structure with a wall number of 7 and an inner diameter of 6 nm.

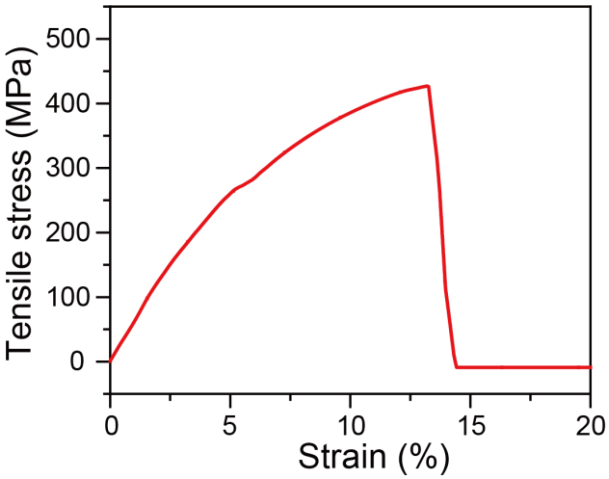

Fig. S3. Mechanical property of the CNT film. The tensile strength was 427 MPa and Young's modulus was 3.2 GPa.

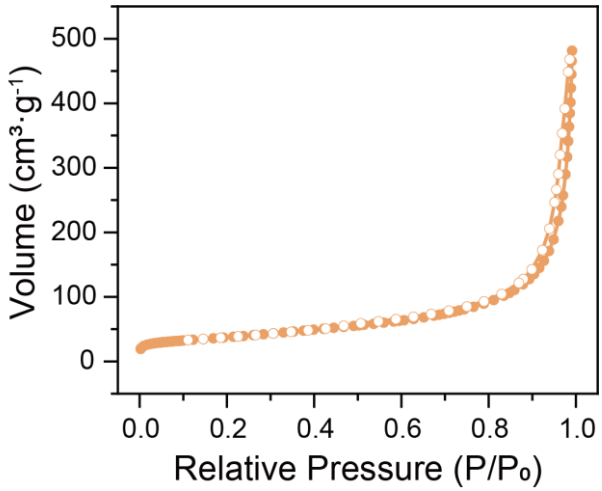

Fig. S4. Nitrogen adsorption-desorption isotherm of the CNT film with a high specific surface area of 134.2 $m^2 \cdot g^{-1}$.

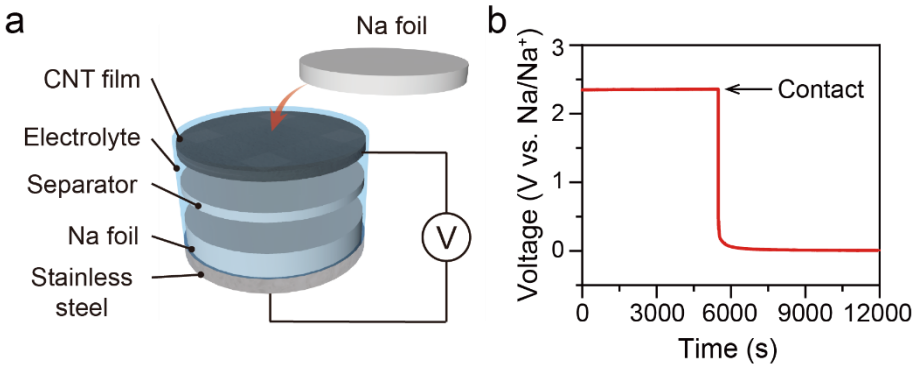

Fig. S5. (a) Schematic of a two-electrode electrochemical cell for monitoring the interaction between CNT film and Na metal. The voltage was on-site recorded when the Na metal was wetted with the electrolyte of 1 M NaTF in diglyme and then pressed on the top of the CNT film. (b) Voltage-time profile of the two-electrode electrochemical cell.

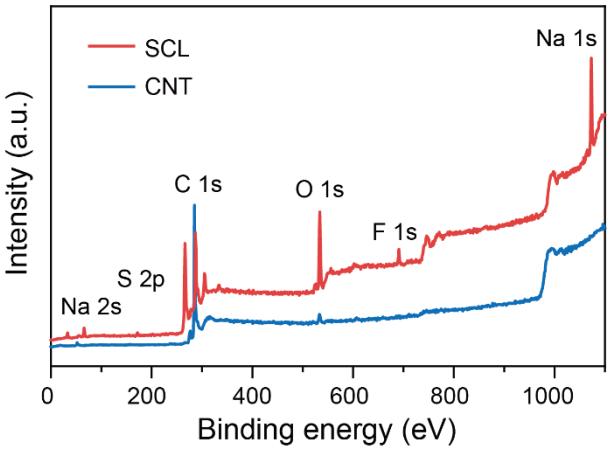

Fig. S6. XPS spectra of pristine CNT film and SCL.

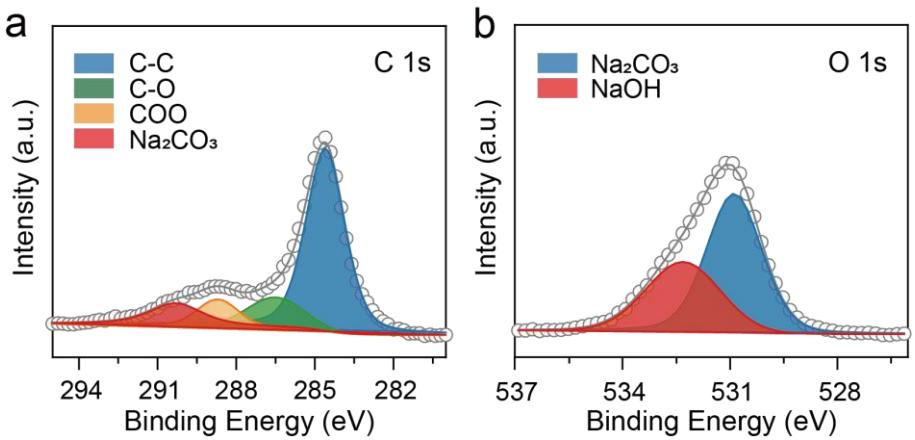

Fig. S7. (a) and (b) High-resolution C 1s and O 1s XPS spectra of solid electrolyte interface (SEI) formed on SCL.

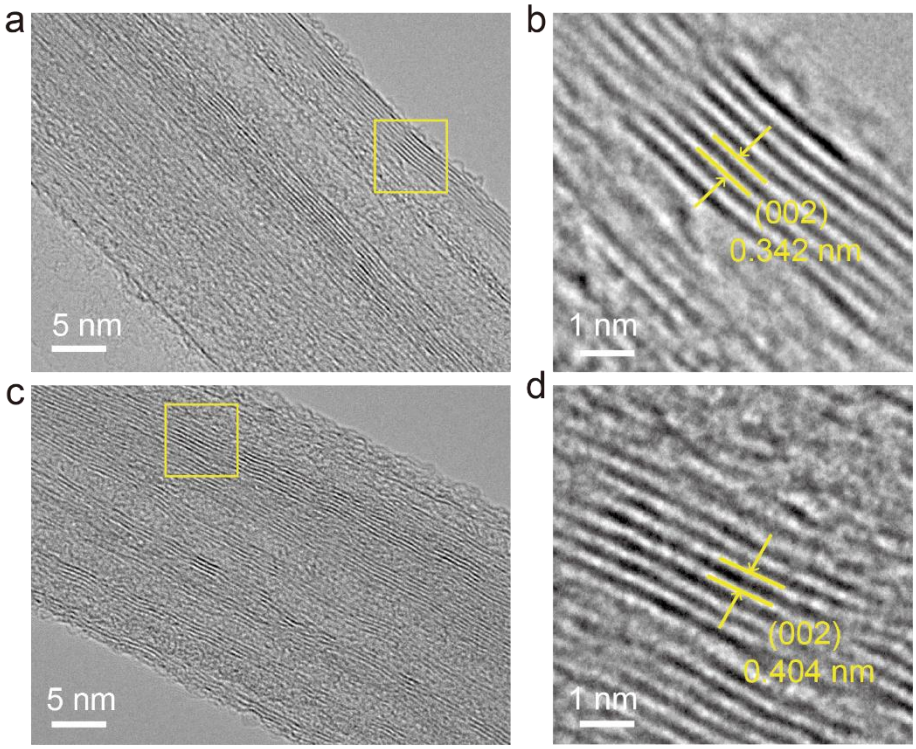

Fig. S8. (a-d) TEM images of the pristine CNT film and SCL, respectively. The average (002) interlayer spacing of the pristine CNT film and SCL were 0.342 and 0.404 nm, confirming Na^+ intercalation into the graphene tubes of CNT after sodiation.

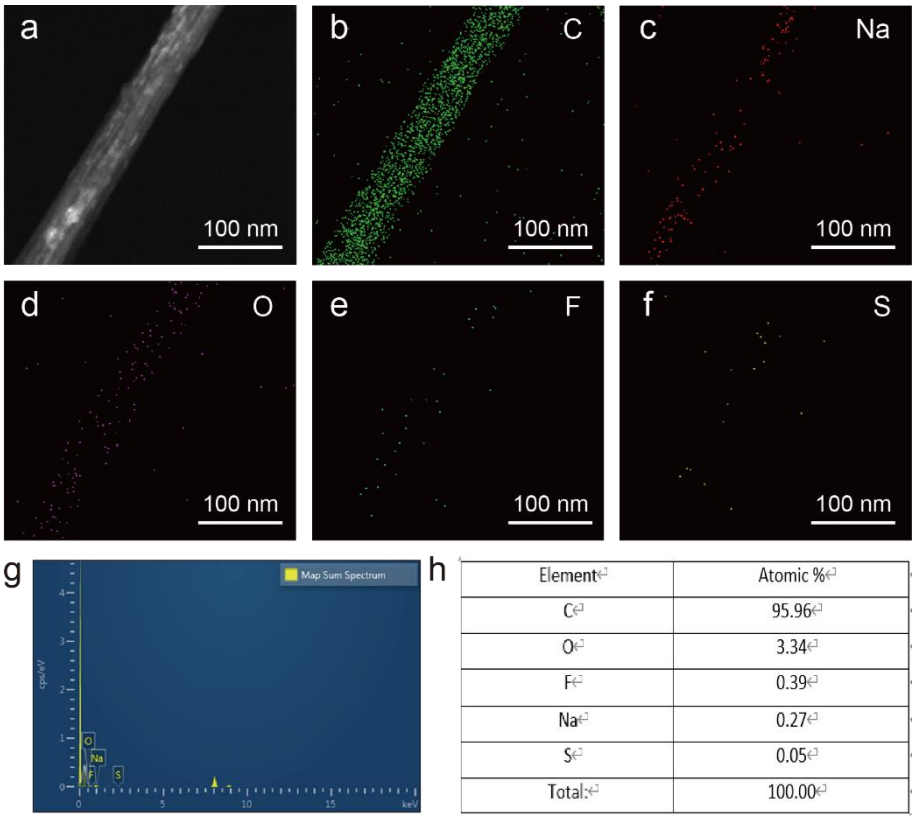

Element	Atomic %
C	95.96
O	3.34
F	0.39
Na	0.27
S	0.05
Total:	100.00

Fig. S9. (a)-(h) TEM images and corresponding elemental mappings of the SCL.

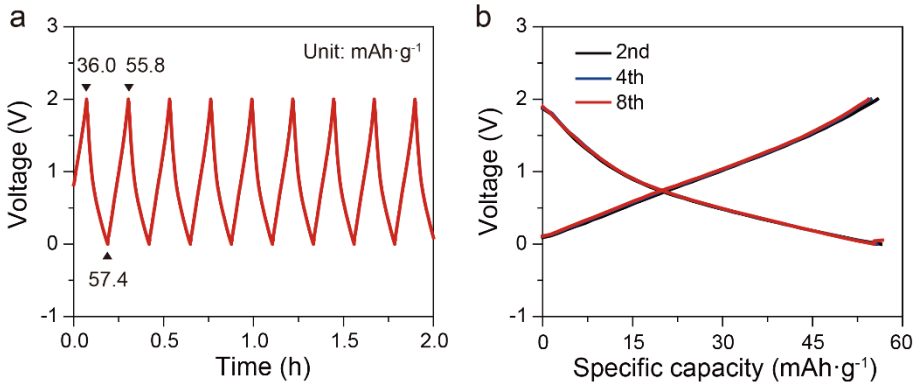

Fig. S10. (a) Voltage-time profiles of the initial forced electrochemical desodiation and the subsequent eight cycles of the Na|SCL half-cells measured at a fixed current of 1 $mA \cdot cm^{-2}$. (b) Charge/discharge voltage profiles of SCL in Na|SCL half-cells.

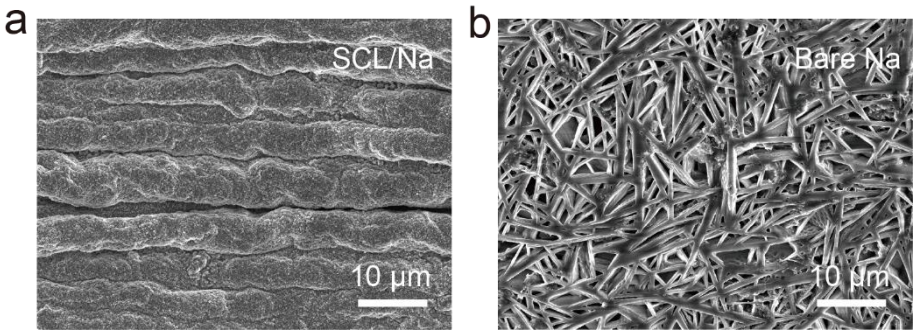

Fig. S11. (a) and (b) Top-view SEM images of SCL/Na and bare Na fiber electrodes after 50 cycles at 5 $mA \cdot cm^{-2}$ and 1 $mAh \cdot cm^{-2}$, respectively.

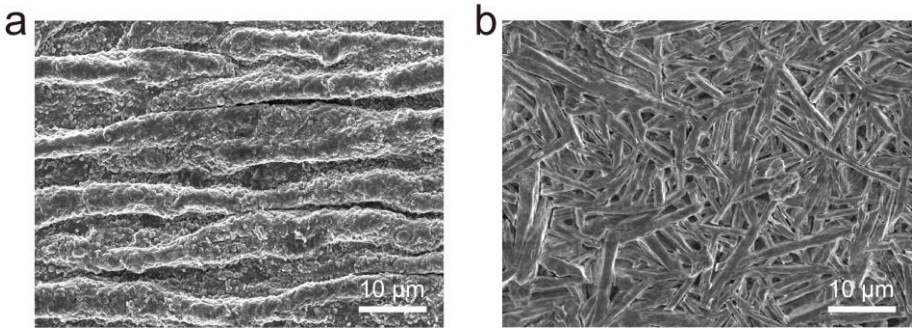

Fig. S12. (a) SEM image of the SCL/Na fiber electrode after 100 cycles at 1 $mA \cdot cm^{-2}$ and 1 $mAh \cdot cm^{-2}$. (b) SEM image of the bare Na fiber electrode disassembled from the dead battery cell with a cycling life less than 80 cycles at 1 $mA \cdot cm^{-2}$ and 1 $mAh \cdot cm^{-2}$.

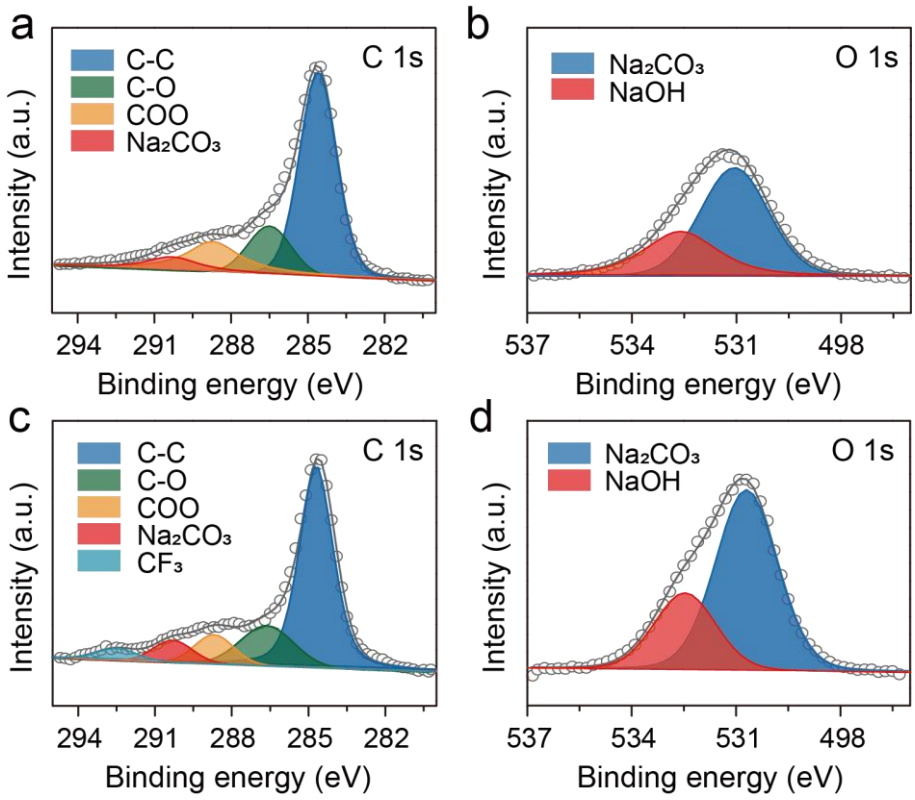

Fig. S13. (a) and (b) High-resolution C 1s and O 1s XPS spectra of SEI on SCL/Na fiber electrode after 50 cycles at 5 mA·cm^{-2} and 1 mAh·cm^{-2}. (c) and (d) High-resolution C 1s and O 1s XPS spectra of SEI on bare Na fiber electrode after 50 cycles at 5 mA·cm^{-2} and 1 mAh·cm^{-2}. The binding energy values were calibrated with the C 1s peak at 284.6 eV. The detailed composition of SEI were compared at **Table S2**.

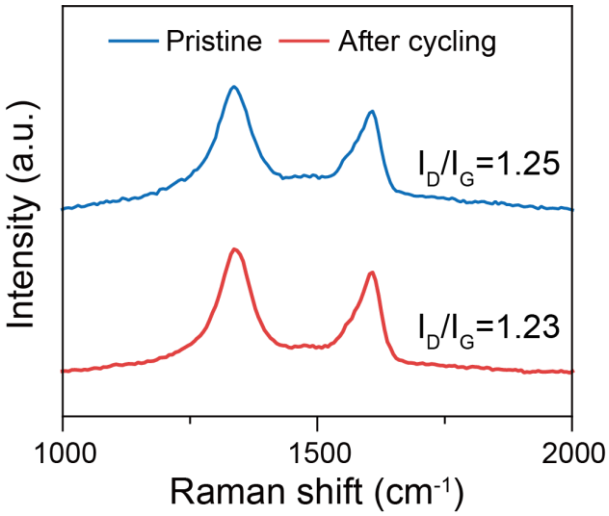

Fig. S14. Raman spectra of SCL before and after 50 cycles at 5 mA·cm^{-2} and 1 mAh·cm^{-2}. The intensity ratio of D to G band was 1.23 that was nearly the same with that of the pristine SCL at 1.25.

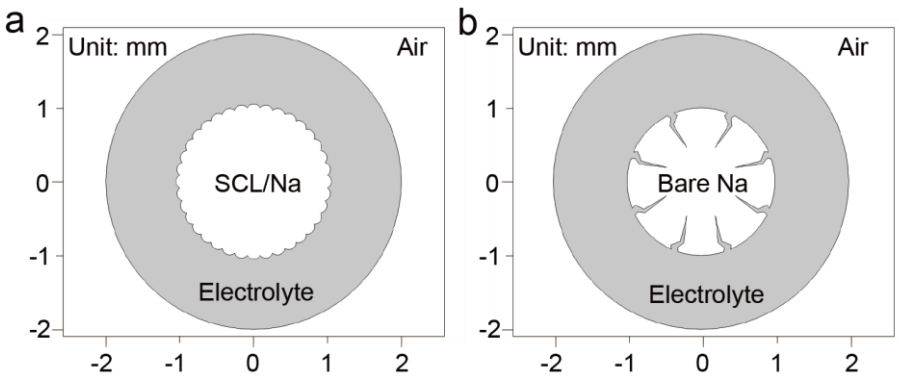

Fig. S15. (a) Simulation cell geometry for SCL/Na–air fiber batteries. The wavy line indicated the robust interface between SCL and Na anode. (b) Simulation cell geometry in COMSOL for bare Na-air fiber batteries. The sharp protrusions indicated the cracks formed on the Na fiber electrode during deformations. The radius of Na fiber anode and the thickness of gel electrolyte were both set as 1 mm.

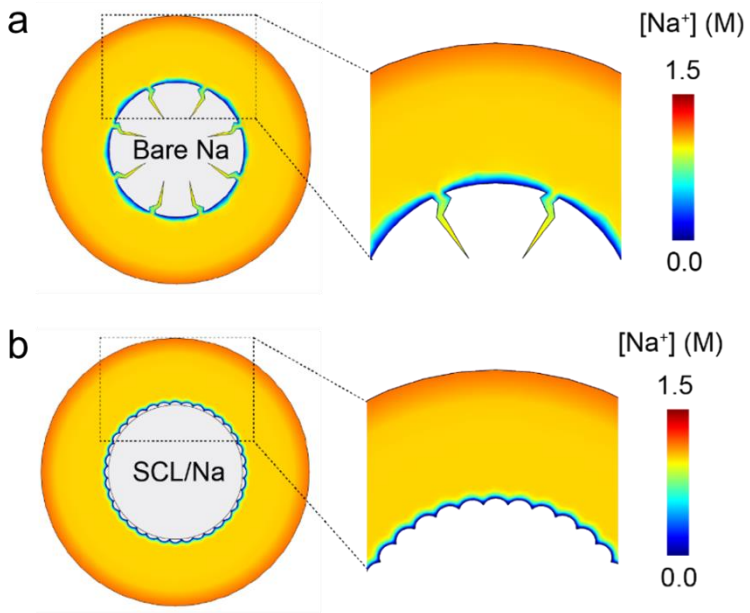

Fig. S16. (a) and (b) Concentration distributions of Na^+ in bare Na-air and SCL/Na–air fiber batteries during charging, respectively. The Na^+ distributed uniformly on the surface of SCL/Na fiber anode during charging. In contrast, Na^+ accumulated around the cracks and distributed unevenly on the surface of bare Na fiber anode, leading to severe local dendrite growth.

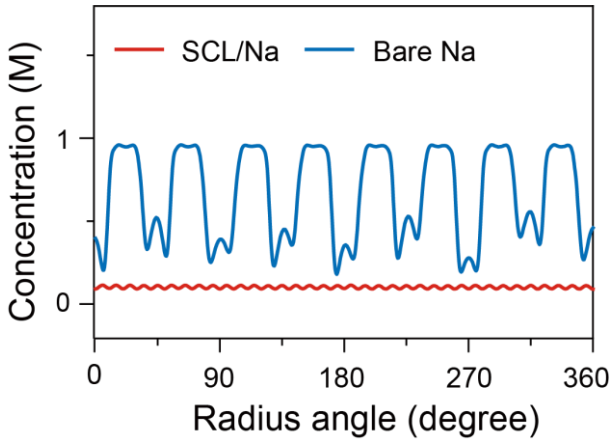

Fig. S17. Na^+ concentration profiles along the SCL/Na and bare Na surface extracted from **Fig. S16**.

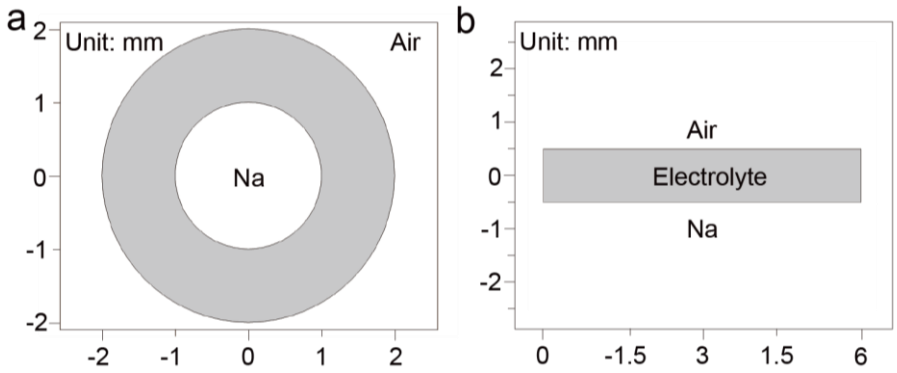

Fig. S18. (a) and (b) Simulation cell geometries of Na–air fiber and planar batteries, respectively. For the Na–air fiber battery, the radius of Na fiber anode and the thickness of gel electrolyte were both set as 1 mm. For the Na-air planar battery, the thickness of gel electrolyte was set as 1 mm.

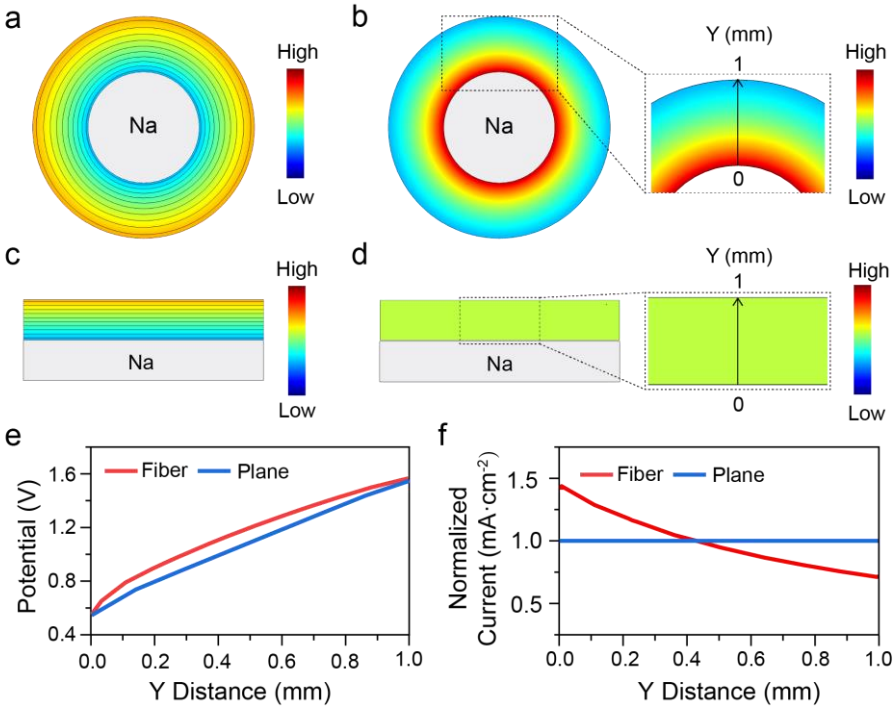

Fig. S19. (a) and (b) Electric field and current density distributions of Na–air fiber batteries, respectively. (c) and (d) Electric field and current density distributions of Na–air planar batteries, respectively. (e) and (f) Electric potential and current profiles of Na-air fiber and planar batteries along Y direction, respectively. The electric field was radically intensified toward inner Na fiber anode, but distributed uniformly in planar battery. The resulting current density on the Na fiber anode was higher than that on Na planar anode, which further aggravated dendritic Na deposition. Therefore, to improve the performance of Na-air fiber battery, it was challenging and essential to disperse the current density and suppress the Na dendrite growth.

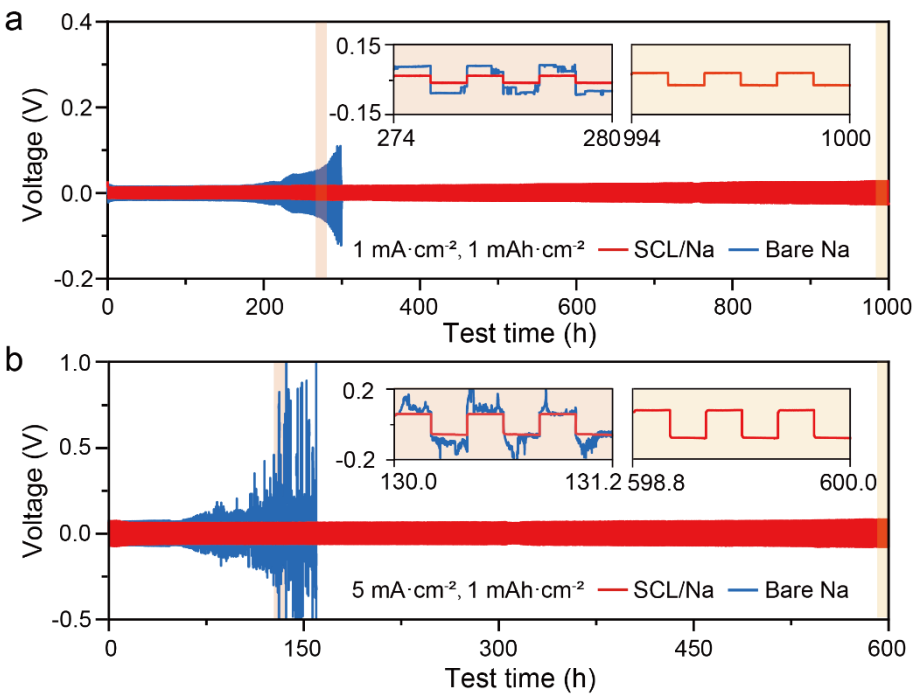

Fig. S20. (a) and (b) Galvanostatic cycling profiles of SCL/Na and bare Na fiber electrodes at 1 mA·cm^{-2} and 1 mAh·cm^{-2}, 5 mA·cm^{-2} and 1 mAh·cm^{-2}, respectively.

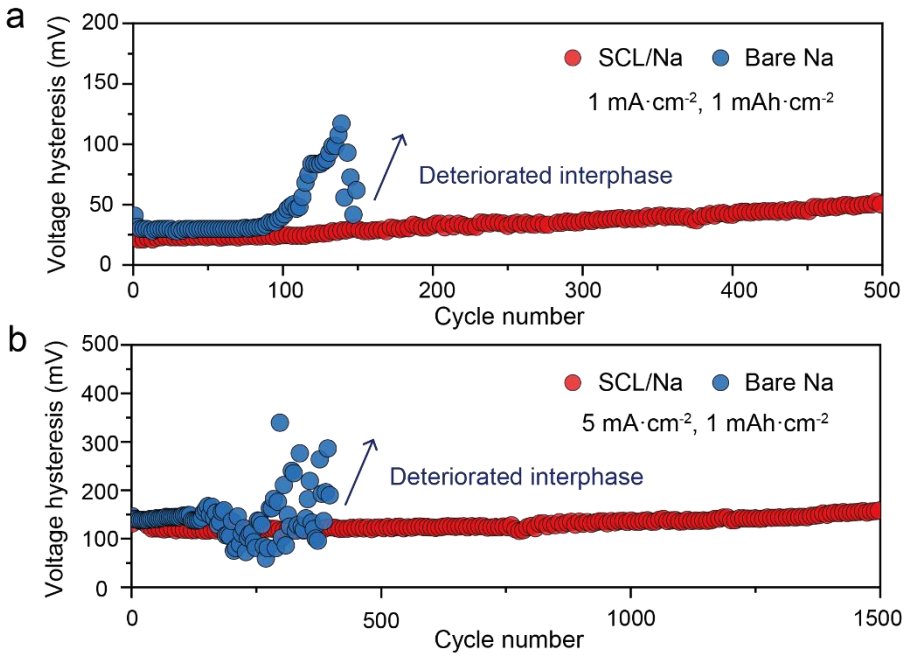

Fig. S21. (a) and (b) Voltage hysteresis of SCL/Na and bare Na fiber electrodes at 1 $mA \cdot cm^{-2}$ and 1 $mAh \cdot cm^{-2}$, 5 $mA \cdot cm^{-2}$ and 1 $mAh \cdot cm^{-2}$, respectively.

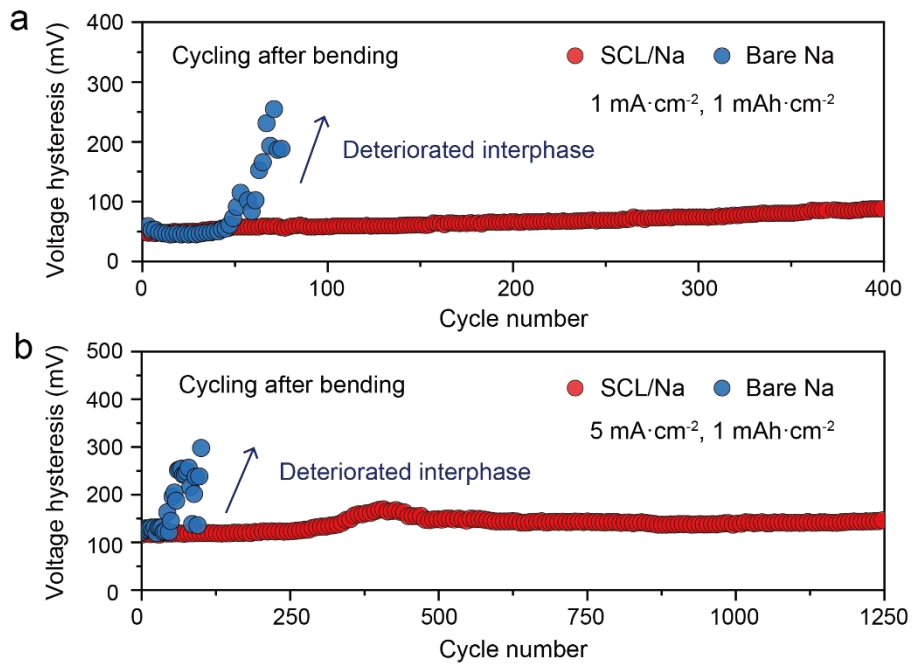

Fig. S22. (a) and (b) Voltage hysteresis of SCL/Na and bare Na fiber electrodes after bending at 1 mA·cm^{-2} and 1 mAh·cm^{-2}, 5 mA·cm^{-2} and 1 mAh·cm^{-2}, respectively.

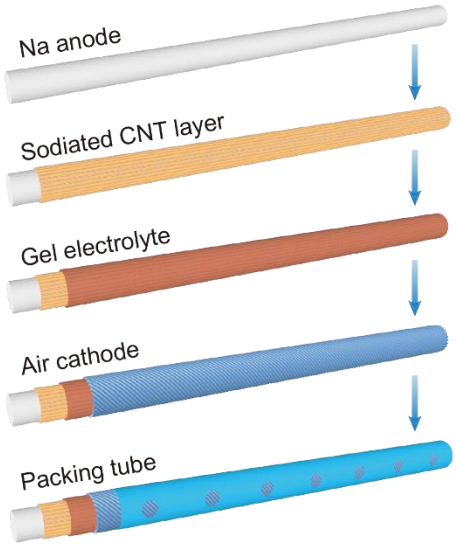

Fig. S23. Schematic illustration of the fabrication procedure of a SCL/Na–air fiber battery.

Fig. S24. Photograph of the SCL/Na–air fiber battery that exhibited a typical diameter of ~0.5 cm and a length of ~15 cm.

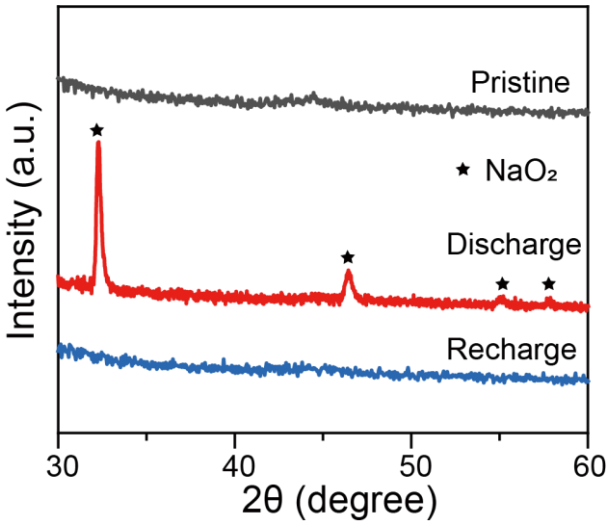

Fig. S25. XRD patterns of the air cathode at pristine, discharging and recharging states.

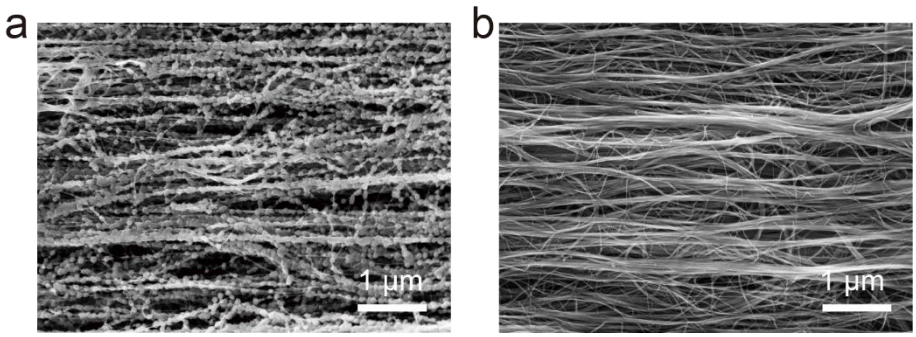

Fig. S26. SEM images of the air cathode after discharging (a) and recharging (b).

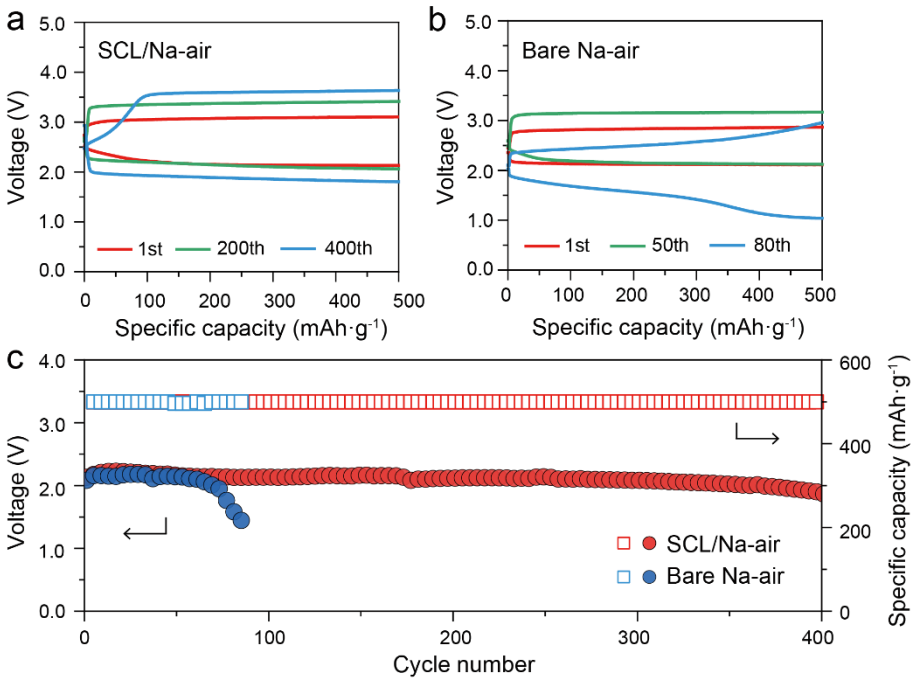

Fig. S27. (a) and (b) Galvanostatic discharge and charge curves of Na–air fiber batteries with SCL/Na and bare Na anodes at 1,000 $mA \cdot g^{-1}$ and 500 $mAh \cdot g^{-1}$, respectively. (c) The corresponding cycling performances of two types of Na–air fiber batteries.

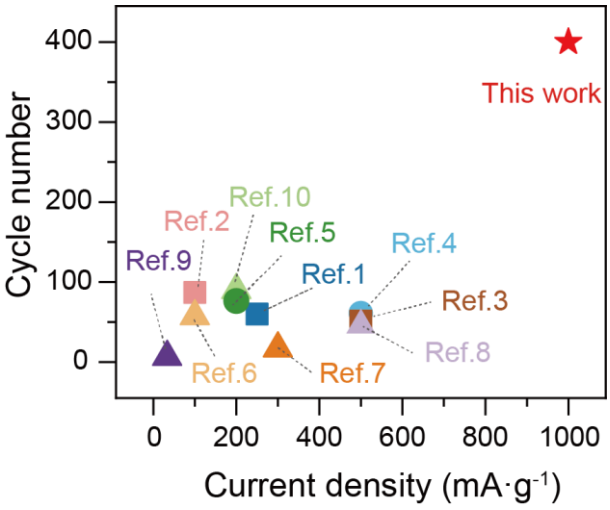

Fig. S28. Comparisons of current density and cycle life of the Na–air fiber battery (★) with reported Na–air batteries based on different modification strategies of anode (■), electrolyte (●), and cathode (▲).

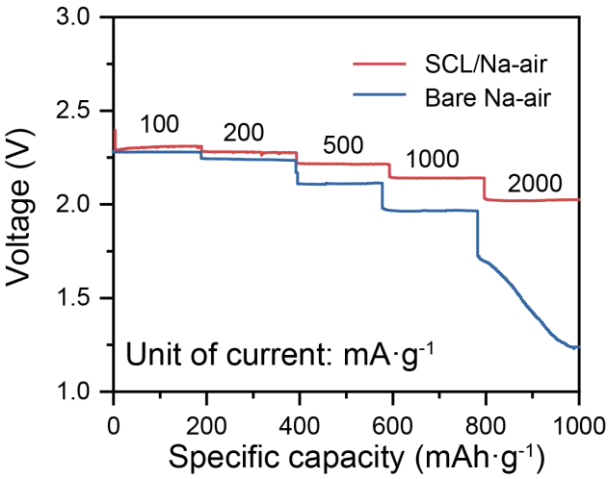

Fig. S29. Rate performance of Na–air fiber batteries with SCL/Na and bare Na anodes.

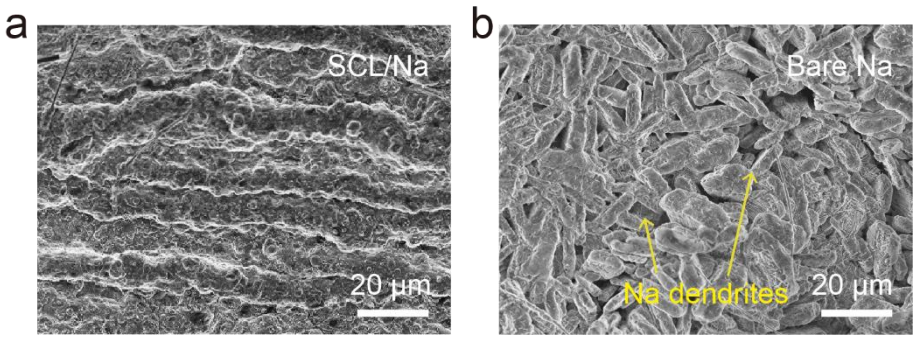

Fig. S30. (a) and (b) SEM images of SCL/Na and bare Na fiber anodes extracted from the Na-air batteries after cycling.

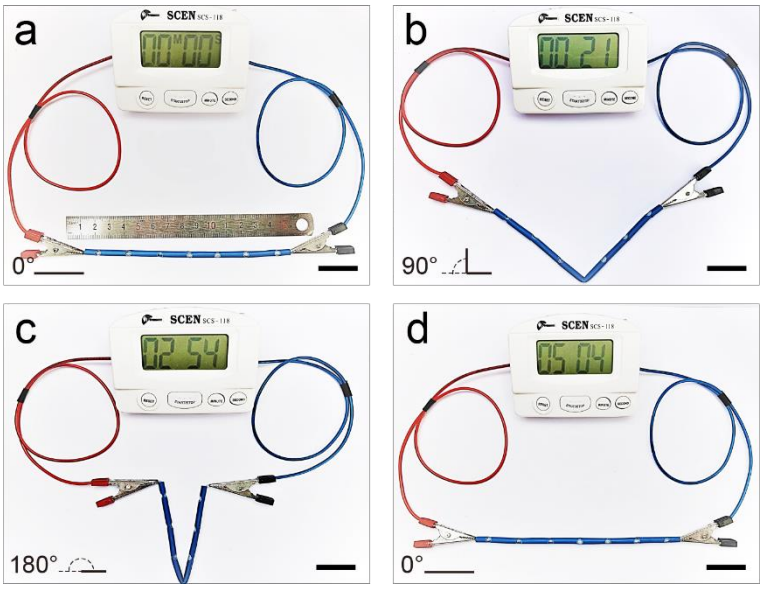

Fig. S31. (a)-(d) Photographs of Na–air fiber battery at different angles from 0° to 180° to power a timer. Scale bars: 2 cm.

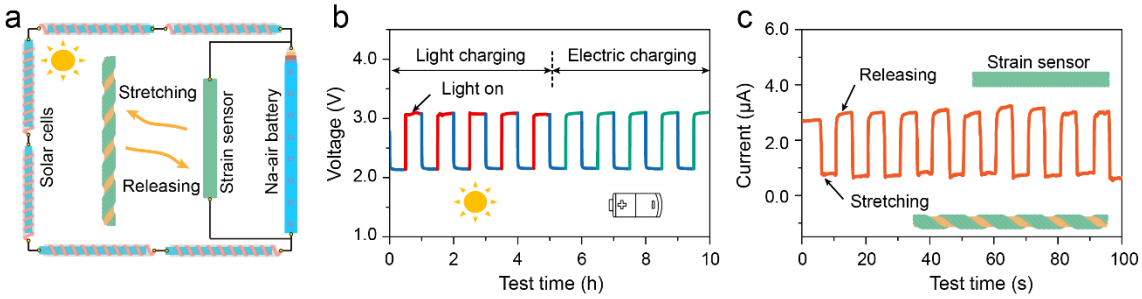

Fig. S32. (a) Schematic illustration of a flexible self-powering system consisting of six fiber solar cells, a Na-air fiber battery, and a fiber strain sensor. (b) Charge-discharge curves of a SCL/Na-air fiber battery photocharged by six fiber solar cells (red line) and charged by external power source (green line). (c) The repeated dynamic response performance of a strain sensor powered by a SCL/Na–air fiber battery.

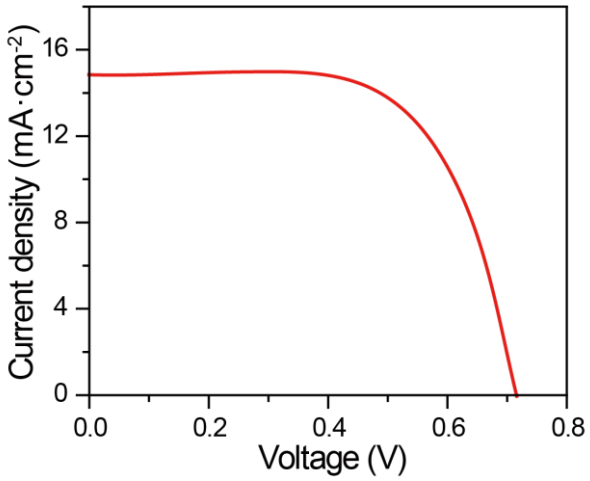

Fig. S33. J-V curve of the fiber dye-sensitized solar cell. The open voltage was 0.733 V. The short circuit current density was 18.82 $mA \cdot cm^{-2}$. The full factor was 0.63. The power conversion efficiency was 8.74%.

Table S1. Surface composition of SCL and pristine CNT by XPS.

Element	SCL (*at%*)	CNT (*at%*)
C	64.32	96.38
O	23.45	2.98
F	2.61	0.15
Na	8.11	0.10
S	1.13	0.10

Table S2. Comparison of the SEI composition of SCL/Na and bare Na fiber electrodes after cycling by XPS.

Element	SCL/Na (*at%*)	Bare Na (*at%*)
C	55.11	42.14
O	26.21	24.67
F	4.54	12.94
Na	12.73	13.55
S	1.42	4.57

Table S3. Comparison of the current density and cycling performance of Na–air fiber battery in this work with previous reports.

Strategy	Current density ($mA \cdot g^{-1}$)	Cycle number	Flexibility	Ref.
Na/CP anode	250	60	Rigid	1
f-PVDF interlayer	100	87	Rigid	2
FEC passivated Na	500	50	Rigid	3
TBA^+ additive electrolyte	500	60	Rigid	4
4% SiO_2 $NaClO_4$/G_4 PVDF-HFP gel electrolyte	200	80	Rigid	5
Co_3O_4@carbon textiles	100	60	Rigid	6
CNT@Co_3O_4	300	21	Rigid	7
NCNT-PAN	500	46	Rigid	8
Pd/ZnO/C	33.3	9	Rigid	9
Co@NCNT Cathode	200	112	Rigid	10
SCL/Na–air fiber battery	1000	400	Flexible	This work

References

[1] X. Lin, Q. Sun, H. Yadegari, X. Yang, Y. Zhao, C. Wang, J. Liang, A. Koo, R. Li, X. Sun, On the cycling performance of Na-O_2 cells: revealing the impact of the superoxide crossover toward the metallic Na electrode, Adv. Funct. Mater. 28 (2018) 1801904.

[2] J. Ma, Y. Yin, T. Liu, X. Zhang, J. Yan, Q. Jiang, Suppressing sodium dendrites by multifunctional polyvinylidene fluoride (PVDF) interlayers with nonthrough pores and high flux/affinity of sodium ions toward long cycle life sodium oxygen-batteries, Adv. Funct. Mater. 28 (2018) 1703931.

[3] S. Wu, Y. Qiao, K. Jiang, Y. He, S. Guo, H. Zhou, Tailoring sodium anodes for stable sodium–oxygen batteries, Adv. Funct. Mater. 28 (2018) 1706374.

[4] S. Zhao, C. Wang, D. Du, L. Li, S. Chou, F. Li, J. Chen, Bifunctional effects of cation additive on Na-O2 batteries, Angew. Chem. Int. Ed. 60 (2021) 3205.

[5] J. Wang, Y. Ni, J. Liu, Y. Lu, K. Zhang, Z. Niu, J. Chen, Room-temperature flexible quasi-solid-state rechargeable Na–O_2 batteries, ACS Cent. Sci. 6 (2020) 1955-1963.

[6] N. Li, D. Xu, D. Bao, J. Ma, X. Zhang, A binder-free, flexible cathode for rechargeable Na-O2 batteries, Chinese J. Catal., 37 (2016) 1172-1179.

[7] Q. Sun, J. Liu, X. Li, B. Wang, H. Yadegari, A. Lushington, M. Banis, Y. Zhao, W. Xiao, N. Chen, J. Wang, T. Sham, X. Sun, Atomic layer deposited non-noble metal oxide catalyst for sodium–air batteries: tuning the morphologies and compositions of discharge product, Adv. Funct. Mater. 27 (2017) 1606662.

[8] Q. Sun, J. Liu, B. Xiao, B. Wang, M. Banis, H. Yadegari, K. R. Adair, R. Li, X. Sun, Visualizing the oxidation mechanism and morphological evolution of the cubic-shaped superoxide discharge product in Na–air batteries, Adv. Funct. Mater. 29 (2019) 1808332.

[9] L. Ma, D. Zhang, Y. Lei, Y. Yuan, T. Wu, J. Lu, K. Amine, High-capacity sodium peroxide based Na–O2 batteries with low charge overpotential via a nanostructured catalytic cathode, ACS Energy Lett. 3 (2018) 276-277.

[10] J. Ma, F. Meng, D. Xu, X. Zhang, Co-embedded N-doped carbon fibers as highly efficient and binder-free cathode for Na–O_2 batteries, Energy Stor. Mater. 6 (2017) 1-8.